RSC Advances

PAPER

View Article Online
View Journal | View Issue

Cite this: *RSC Adv.*, 2023, **13**, 35018

Interlayer coupling controlled electronic and magnetic properties of two-dimensional $VOCl_2$/$PtTe_2$ van der Waals heterostructure

Zhonghua Qian, † Jie Ji,† Liyan Qian,† Yuxuan Mao, Suchen Yao, Jingyi Xu and Licheng Wang*

Received 24th October 2023
Accepted 26th November 2023

DOI: 10.1039/d3ra07237a

rsc.li/rsc-advances

The coupling of hetero monolayers into van der Waals (vdW) heterostructures has become an effective way to obtain tunable physical and chemical properties of two dimensional (2D) materials. In this work, based on first principles calculations, we systematically explore the electronic and magnetic properties of a 2D $VOCl_2$/$PtTe_2$ heterostructure. Our results indicate that the ground state of the $VOCl_2$/$PtTe_2$ heterostructure is a ferromagnetic (FM) metal with large magnetic anisotropy energy, among which, the $VOCl_2$ "sublayer" shows FM half metallic properties while the $PtTe_2$ "sublayer" shows nonmagnetic metallic properties. The Curie temperature (T_C) of $VOCl_2$/$PtTe_2$ is 111 K. Moreover, the FM–antiferromagnetic (AFM) phase transition can be obtained under biaxial strain. Our work provides an effective way to improve the performance of 2D monolayers in nano-electronic devices.

Introduction

Compared to conventional electronics based on charge, spintronics, also called spin transport electronics or spin-based electronics, have drawn great attention due to their coupling control of charge and spin,[1–4] in which the electron spin carries information and offers opportunities for a new platform of designing devices combining standard microelectronics with spin-dependent effects that arise from the interaction between the spin of the carrier and the magnetic properties of the material. Since the discovery of graphene, two dimensional (2D) materials have been a booming topic in recent decades, such as transition metal dichalcogenides (TMDs), phosphorus, silicene, borophene, *etc.*[5–7] However, most of the 2D materials are nonmagnetic, which hinders their application in spintronic devices due to the lack of spin degrees of freedom. Therefore, searching for 2D materials with intrinsic magnetism is an urgent need. Fortunately, the field is evolving rapidly and many exciting developments in 2D materials science have occurred, and the rise of ferromagnetic (FM) or antiferromagnetic (AFM) candidates has provided one new platform for the applications of 2D spintronics at the nanoscale. Since the exfoliation of the ferromagnetic (FM) CrI_3 monolayer[8] and $Cr_2Ge_2Te_6$ monolayer[9] from their van der Waals bulks in 2017, a number of 2D magnetic materials have been synthesized experimentally or predicted theoretically to date, such as TMDs or trichalcogenides MX_i (M = Cr, Mn, Ni, Ru; X = Cr, Br, I; i = 2, 3),[10–21] MPX_3 (M = Fe, Ni, Mn, Co, Zn; X = S, Se),[22–27] MOX (M = Fe, Cr, V, Ti; X = Cl, Br, I),[28,29] and TM borides TM_xB_y (x, y = 1, 2; y = 3, 4, 6),[30–32] *etc.*, which display rich magnetic configurations, magnetoelectric coupling effects, and magnetoresistance properties.

However, the potential application of 2D magnetic materials in practical electronic devices still faces two main challenges; one is that the categories of 2D materials with intrinsic FM or AFM properties are rare. The other one is that the Curie temperature (T_C) or Néel temperature (T_N) of these 2D magnetic materials are far lower than room temperature, which impedes their application in spintronic devices. For examples, the T_Cs for the FM CrI_3 monolayer, bilayer $Cr_2Ge_2Te_6$ and Fe_3GeTe_2 monolayer are only 45 K, 40 K and 130 K, respectively. On the other hand, 2D AFM candidates are much more common in nature, which has become the complements of FM based spintronic devices due to their advantages that AFM materials are insensitive to external magnetic field and more common in reality,[33] which enable them to be promising in practical application. However, one difficulty towards the application of 2D AFM candidates in spintronics is the vanishing of macroscopic magnetic moments in conventional antiferromagnets, which induces unpolarized conduction electrons. Thus, the generation of high spin polarization states in 2D antiferromagnets provides new opportunities to improve their performance in spintronics.

To date, many efforts regarding the precise regulation of spin configurations of 2D materials have been made, and various approaches have been proposed, such as applying electric field,[16,34] exerting external strains,[35–37] doping,[38–41] and

College of Physics Science and Technology & Microelectronics Industry Research Institute, Yangzhou University, Yangzhou 225002, China. E-mail: mx120200330@yzu.edu.cn

† Zhonghua Qian, Jie Ji and Liyan Qian contribute equally to this work.

constructing heterostructure,[42–45] and so on. Especially, the heterostructure engineering has become popular in recent years due to its valid regulation without extra consumption. For example, in 2022, Guo *et al.* revealed that the magnetic phase of monolayer NiI_2 can undergo the switching of AFM state to FM state by reversing the polarization direction of ferroelectric In_2Se_3 layer, which leads to the spin-polarized/unpolarized current in the FM/AFM state.[46] Yang *et al.* found that when the layers of the GaN increase, the band alignment of $CrBr_3$/GaN heterostructure can be transformed from type-I to type-II.[47] In 2023, Guo *et al.* demonstrated that the magnetic state of $MnPS_3$/$MnCl_3$ can be changed from AFM to FM by reducing the interlayer distance, and the electronic properties can also be modulated by the interlayer distance.[48] Nonetheless, people's efforts to manipulate the spins states of AFM materials are rare.

In this work, we systematically studied the structure, electronic and magnetic properties of 2D $VOCl_2$/$PtTe_2$ heterostructure composed of AFM $VOCl_2$ semiconductor and nonmagnetic $PtTe_2$ semiconductor. Compared to $VOCl_2$ monolayer and $PtTe_2$ monolayer, the $VOCl_2$/$PtTe_2$ heterostructure is changed to be FM metal, in which the $VOCl_2$ "sublayer" shows FM half metallic property, and $PtTe_2$ "sublayer" shows NM metallic property. Moreover, the Curie temperature of FM $VOCl_2$/$PtTe_2$ is 111 K, and the magnetic anisotropy energy (MAE) of $VOCl_2$/$PtTe_2$ heterostructure is comparable with FeCo alloys. At last, we investigated the magnetic and electronic properties of $VOCl_2$/$PtTe_2$ heterostructure by applying biaxial strains, it is suggested that the heterostructure undergoes a FM metal to AFM metal transition, and the $VOCl_2$/$PtTe_2$ heterostructure can be used for designing field-effect spin filter under tensile strain and compressive strains ($\varepsilon > -1.81\%$).

Materials and methods

All the calculations based on density functional theory (DFT) were performed by Vienna *Ab initio* Simulation Package (VASP) in this work.[49–51] The exchange correlation interaction is described by Perdew–Burke–Ernzerholf (PBE)[52] functional, and the interaction between valence electrons and ion nuclei is described by the projector-augmented wave potential (PAW)[53] method. The cutoff value for plane wave basis set is set to 500 eV. The energy and force convergence criteria are set to be 10^{-6} eV and 0.01 eV $Å^{-1}$, respectively. In our calculation, a vacuum slab as large as 25 Å is applied to avoid the physical interactions of adjacent cells. For geometry optimization and electronic structure calculations, the first Brillouin zone is sampled by Γ-centred k mesh of $7 \times 7 \times 1$ and $15 \times 15 \times 1$. The vdW interaction is considered by using the DFT-D2 method.[54] In order to consider the strong interactions of transition metal atoms' d-electrons, the GGA + U method[55] is adopted with U_{eff} = 3.0 eV to consider the Coulomb and exchange interaction of 3d electrons according to previous studies.[56–58]

Results and discussions

First, we explored the structures and electronic properties of $VOCl_2$ and $PtTe_2$ monolayers. As shown in Fig. 1(a) and (c), the space symmetry groups of $VOCl_2$ and $PtTe_2$ monolayers are *Pmm*2 and *P*3*m*1, respectively, and the lattice constants of them are a/b = 3.44/3.77 Å and a/b = 3.93/3.93 Å, respectively. For $VOCl_2$ monolayer, the V and O atoms sit in one plane, which were sandwiched by two Cl layers, and Cl atoms are in the bridge site of V–V bonds. $PtTe_2$ monolayer has the same structure with 1T-MoS_2 monolayer. Further electronic and magnetic property calculations confirm that $VOCl_2$ monolayer is stripe-style AFM semiconductor with an indirect band gap of 2.0 eV, and $PtTe_2$ monolayer is a nonmagnetic semiconductor with an indirect band gap of 0.46 eV. The structure and electronic properties of both $VOCl_2$ monolayer and $PtTe_2$ monolayer in our calculation are consistent with previous reports,[59,60] indicating that the methods chosen in this work are reasonable. To build the $VOCl_2$/$PtTe_2$ heterostructure, the rectangular lattice of $PtTe_2$ with $\sqrt{3} \times 1 \times 1$ supercell and $2 \times 1 \times 1$ $VOCl_2$ supercell are chosen. The optimized in-plane lattice constant of the heterostructure is 6.88 Å and 3.77 Å along a and b directions, which are same with that of $2 \times 1 \times 1$ $VOCl_2$ supercell. In addition, we calculated the lattice mismatch of $PtTe_2$ monolayer based on

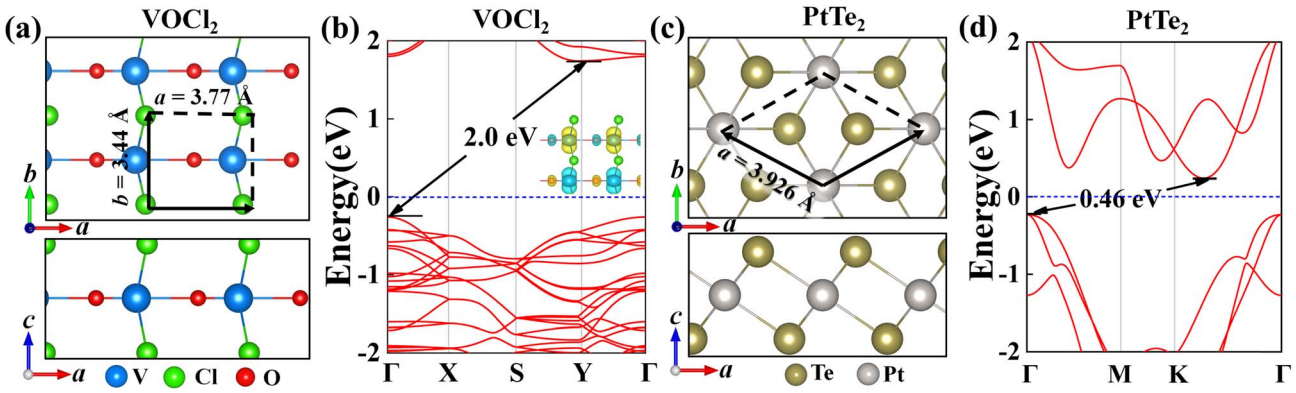

Fig. 1 (a and c) Top and side views of the geometry and band structure of $VOCl_2$ monolayer and $PtTe_2$ monolayer. The unitcell is denoted by the black arrows and the dotted lines. (b and d) The band structures of $VOCl_2$ monolayer and $PtTe_2$ monolayer, insets in (b) are the spin density plot of $VOCl_2$ monolayer.

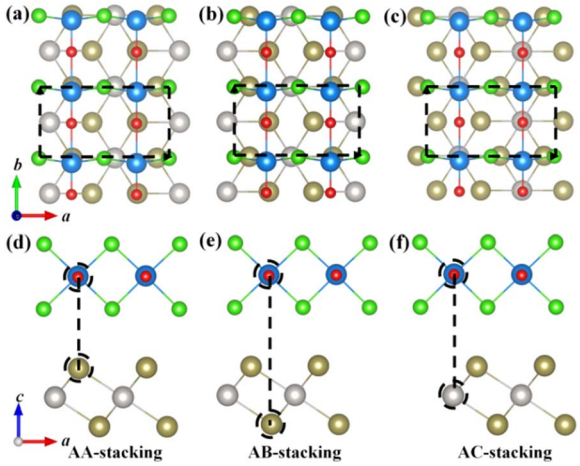

Fig. 2 (a–f) Top and side views of the AA-, AB-, and AC-stacked $VOCl_2/PtTe_2$ heterostructure. The black dotted circles in side view imply that the two atoms are overlapping in top view.

$\xi = \frac{|L_1 - L|}{L} \times 100\%$. Here, L_1 and L represent the lattice constants of $PtTe_2$ monolayer and the heterostructure in the same direction, respectively. The lattice mismatch along a and b directions for $PtTe_2$ sublayer are about 1.16% and 3.98%, respectively, such mismatch is acceptable in 2D heterostructures.

To determine the most stable stacking configuration of $VOCl_2/PtTe_2$ heterostructure, three different stacking styles, that is, AA-, AB-, and AC-stacking, were considered, as shown in the top and side views in Fig. 2. (i) AA-stacking: half of the V atoms in $VOCl_2$ monolayer sit on top of Te atoms facing Cl atoms, as shown in Fig. 2(a) and (d); (ii) half of the V atoms in $VOCl_2$ monolayer sit on top of Te atoms far away from the interface of the heterostructure, as shown in Fig. 2(b) and (e); (iii) half of the V atoms in $VOCl_2$ monolayer sit on top of Pt atoms, as shown in Fig. 2(c) and (f). The results show that the AA stacking configuration is the most stable one, which is about of 0.51 eV per u.c. and 0.59 eV per u.c. lower in energy than that of AB- and AC-stacking configurations, respectively. The interlayer distance between $VOCl_2$ monolayer and $PtTe_2$ monolayer is 3.02 Å, indicating the van der Waals (vdW) interaction of the heterostructure. Based on this analysis, we will only focus on the electronic and magnetic properties of $VOCl_2/PtTe_2$ heterostructure with AA stacking in the following section.

In order to verify the structural stability of the $VOCl_2/PtTe_2$ heterostructure, we calculated the binding energy (E_b) according to eqn (1),

$$E_b = E_{VOCl_2/PtTe_2} - E_{VOCl_2} - E_{PtTe_2}, \quad (1)$$

where $E_{VOCl_2/PtTe_2}$, E_{VOCl_2} and E_{PtTe_2} represent the energy of $VOCl_2/PtTe_2$ heterostructure, $VOCl_2$ monolayer and $PtTe_2$ monolayer, respectively. The calculated binding energy is −0.52 eV, the negative value indicates that the $VOCl_2/PtTe_2$ heterostructure is energetically stable. Such stability of the $VOCl_2/PtTe_2$ heterostructure may arise from the interfacial electrons transfer between the two sublayers, which would occur in 2D vdW heterostructure. Therefore, the charge transfer at the heterostructure interface was examined by calculating the charge density difference (CDD) based on eqn (2),

$$\Delta\rho = \int\rho_{all}(x, y, z) - \int\rho_1(x, y, z) - \int\rho_2(x, y, z), \quad (2)$$

here, the three terms on the right side indicate the charge densities of the $VOCl_2/PtTe_2$ heterostructure, $VOCl_2$ monolayer and $PtTe_2$ monolayer, respectively. The positive and negative values of $\Delta\rho$ indicate charge accumulation and depletion, respectively. As shown in the inset of Fig. 3(e), the charges are redistributed at the interface of the heterostructure. The plane-averaged charge density difference is plotted in the right panel in Fig. 3(e), which has negative/positive charge densities near the $PtTe_2/VOCl_2$ interface, indicating the electron loss/gain of the two sublayers, which are transferred from $PtTe_2$ monolayer to $VOCl_2$ monolayer. In order to better understand interface charge transfer, we calculated the electrostatic potential (see Fig. 3(e)). It can be seen that the potential of $VOCl_2$ monolayer is slightly higher (about 7.37 eV) than that of $PtTe_2$ monolayer, forming an effective electric field from $VOCl_2$ monolayer to $PtTe_2$ monolayer, which results in the fact that electrons transfer from $PtTe_2$ monolayer to $VOCl_2$ monolayer. Such results are consistent with that shown in the plane-averaged charge density difference, to determine the magnetic ground state of $VOCl_2/PtTe_2$ heterostructure, four types of magnetic configurations, that is, one ferromagnetic (FM) and three antiferromagnetic (AFM1, AFM2, AFM3) configurations are considered, as displayed in Fig. 3(a)–(d). Our calculations show that the heterostructure favors FM ground state (see Fig. 3(a)), which is about 0.02 eV, 0.11 eV, and 0.12 eV lower in energy than that of AFM1, AFM2, and AFM3 magnetic states. The spin density plot (Fig. 3(a)) manifests that the magnetic moments of the heterostructure are contributed by the $VOCl_2$ sublayer, while the $PtTe_2$ sublayer is still nonmagnetic. The total magnetic moment of this $VOCl_2/PtTe_2$ heterostructure is 2.16 μ_B per unit cell, which arises mainly from the d orbitals of V atoms and p orbitals of Te atoms. Compared with free standing $VOCl_2$ monolayer, the O atoms goes closer to the middle of the two V atoms and the Cl atoms are closer to the V–O plane, resulting in a change in the V–O bonds from 2.28 Å/1.49 Å to 2.10 Å/1.67 Å, and a change in the V–Cl bonds from 2.67 Å to 2.38 Å, and the Cl–V–Cl bond angle is changed from 80.27° to 92.63°. According to the Goodenough–Kanamori–Anderson (GKA) rule,[61–63] superexchange interaction with the angle between TM–B–TM close 90° favors FM magnetic ordering. In $VOCl_2/PtTe_2$ heterostructure, the V–Cl–V bond angle is 91.88°, which is closer to 90° than that in free standing $VOCl_2$ monolayer of 80.27°, such variation may strengthens the ferromagnetic coupling, leading to the FM ground state in the $VOCl_2/PtTe_2$ heterostructure. The Bader charge analysis shows that the average charges on V/O atom are 3.30 electrons and 6.78 electrons in the $VOCl_2/PtTe_2$ heterostructure, respectively, which are larger/smaller than that in free standing $VOCl_2$ monolayer of −0.11 e/0.20 e. Such electron redistribution of $VOCl_2$ monolayer originates from the interlayer interaction, as mentioned above, electrons transfer

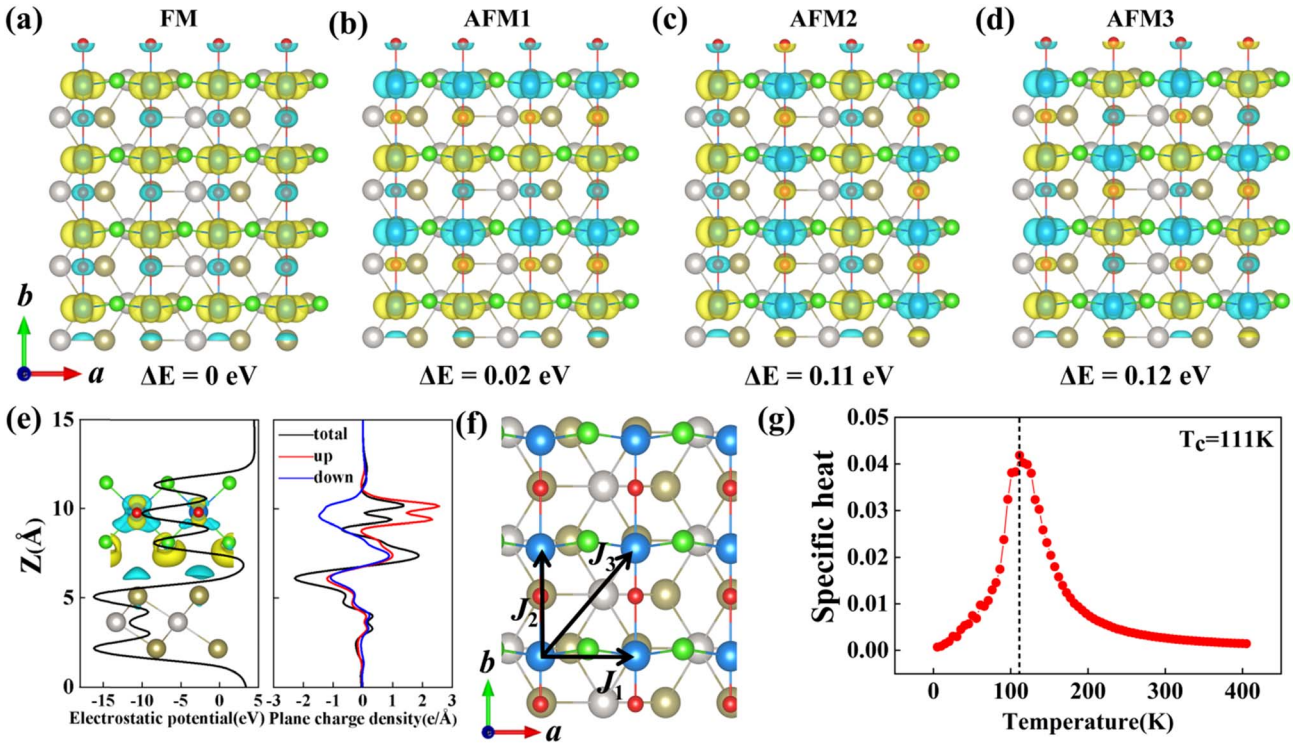

Fig. 3 (a–d) FM configuration and three AFM configurations. Yellow and blue colours represent up and down spins, respectively. (e) Electrostatic potential and plane-averaged charge density difference along the z-direction, inset in electrostatic potential is the CDD plot, black, red, and blue lines in plane-averaged charge density difference denote the total, spin-up, and spin-down charge densities, respectively. (f) Magnetic configuration for estimating the exchange-interaction constants of $VOCl_2/PtTe_2$ heterostructure. J_1, J_2 and J_3 represents the intralayer and interlayer spin-exchange parameters. (g) The specific heat (C_V) as a function of the temperature.

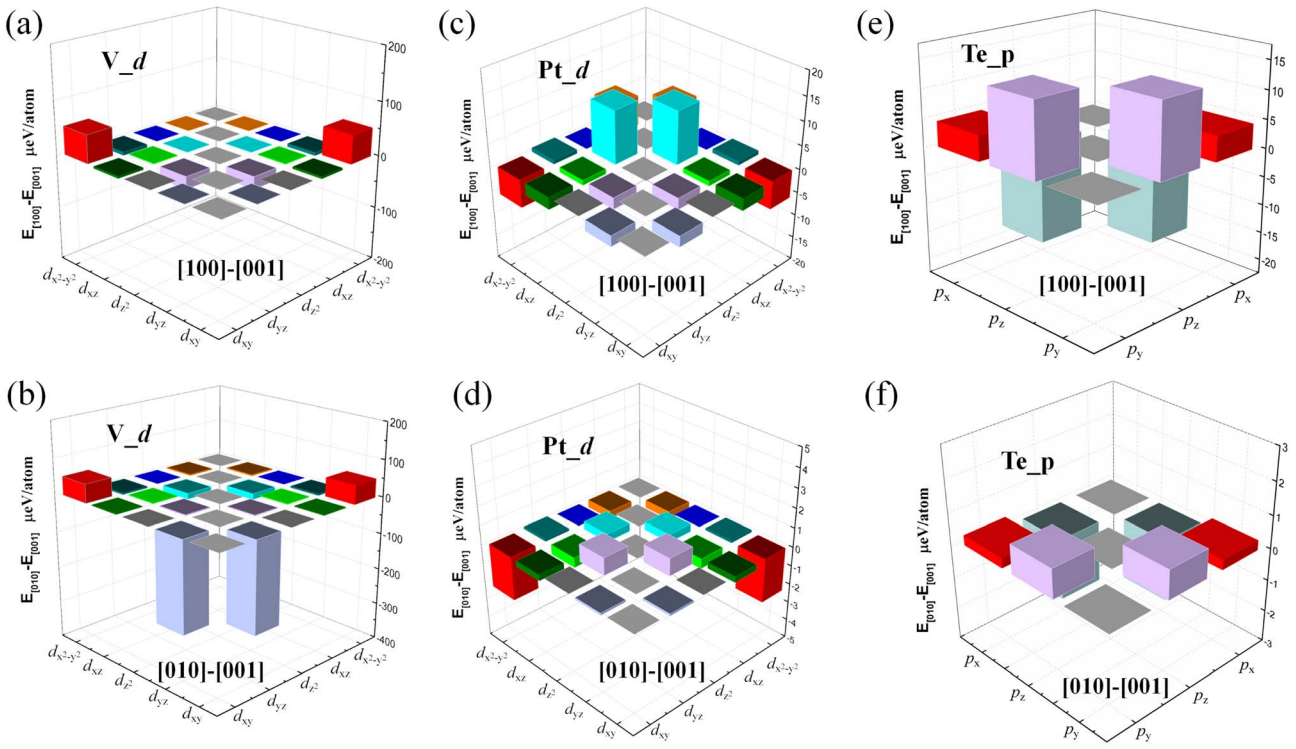

Fig. 4 The contribution to MAE from the SOC interaction between different V-d, Pt-d and Te-p orbital atoms along the [100] and the [010] directions. The energy is the reference along the [001] direction.

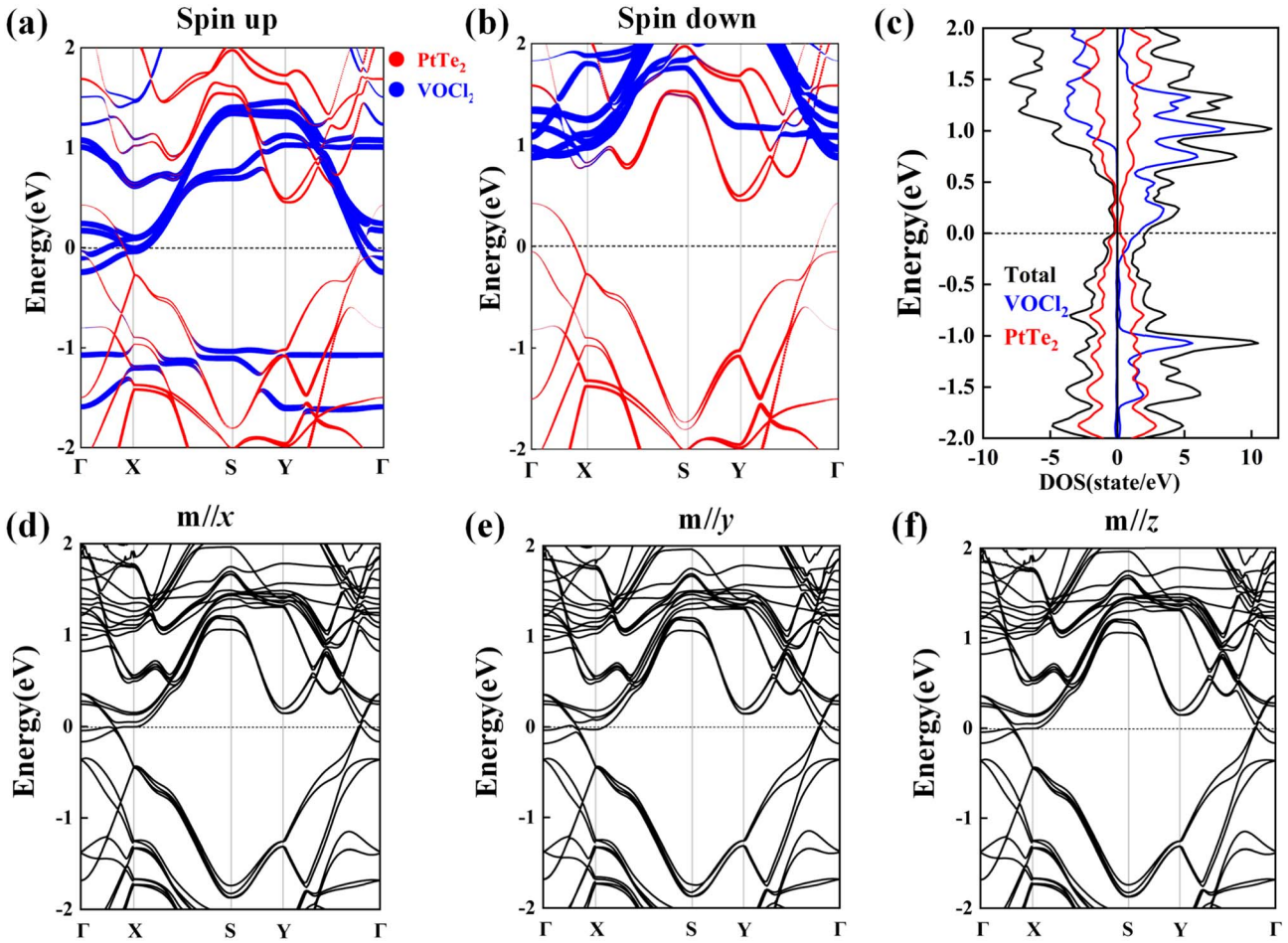

Fig. 5 (a and b) Spin polarized band structures and (c) density of states (DOS) of $VOCl_2/PtTe_2$ heterostructure, in which the bands from $PtTe_2$ and $VOCl_2$ sublayers are denoted by red and blue lines, respectively. (d–f) Band structures of $VOCl_2/PtTe_2$ considering SOC effect with the magnetization direction along *x*, *y*, and *z* directions, respectively.

from $PtTe_2$ monolayer to $VOCl_2$ monolayer. The partially filled p orbitals in the O anions are responsible for the local magnetic moment of -0.158 μ_B and -0.172 μ_B in $VOCl_2/PtTe_2$ heterostructure.

Next, we calculated the MAE to investigate the stability of the 2D FM order in the $VOCl_2/PtTe_2$ heterostructure. By considering spin orbital coupling (SOC), we calculated the energies of the heterostructure with magnetization along *x*, *y* and *z* positive directions. The results show that the system hosts the lowest energy when the magnetization is along the *y* axis, which is about 0.84 meV and 0.78 meV lower than that of along *x* and *z* axis positive directions, respectively, indicating the easy magnetization axis is in-plane and the MAE value is 0.84 meV, such MAE value is comparable with that in FeCo alloys, which is promising magnetic recording media.[64] Fig. 4 shows the amount of energy change in the [100], [010] and [001] directions for individual V-d and Pt-d orbitals. It is revealed that the hybridization between V-d_{yz} and d_{xy} orbitals and that between V-d_{yz} and V-$d_{x^2-y^2}$ contribute mainly to the MAE. In addition, the energy changes of individual Pt-d and Te-p orbitals are within 15 μeV. Furthermore, we calculate the Curie temperature (T_C) of FM $VOCl_2/PtTe_2$ heterostructure using Monte Carlo (MC) simulations based on the Heisenberg model, which is a critical characteristic regarding the application of 2D FM materials in spintronic devices. The Heisenberg spin Hamiltonian is written as

$$H = -\sum_{k=1,2,3} J_k \sum_{i \neq j} S_i \cdot S_j - \sum_i A_i {S_{iz}}^2, \quad (3)$$

here, S_i is the spin operator of each V atom. A_i is the MAE index. J_k is the magnetic interaction index between the V atom. We consider the nearest neighbour (J_1), the second nearest neighbour (J_2), and the third nearest neighbour (J_3) (Fig. 3(f)), whose values can be extracted from the following equations,

$$E_{FM} = E_0 - (J_1 + J_2 + 2J_3)|S|^2 - A|S|^2 \quad (4)$$

$$E_{AFM1} = E_0 - (-J_1 + J_2 - 2J_3)|S|^2 - A|S|^2 \quad (5)$$

$$E_{AFM2} = E_0 - (J_1 - J_2 - 2J_3)|S|^2 - A|S|^2 \quad (6)$$

$$E_{AFM3} = E_0 - (-J_1 - J_2 + 2J_3)|S|^2 - A|S|^2 \quad (7)$$

The exchange parameters (J_1, J_2 and J_3) can be derived as:

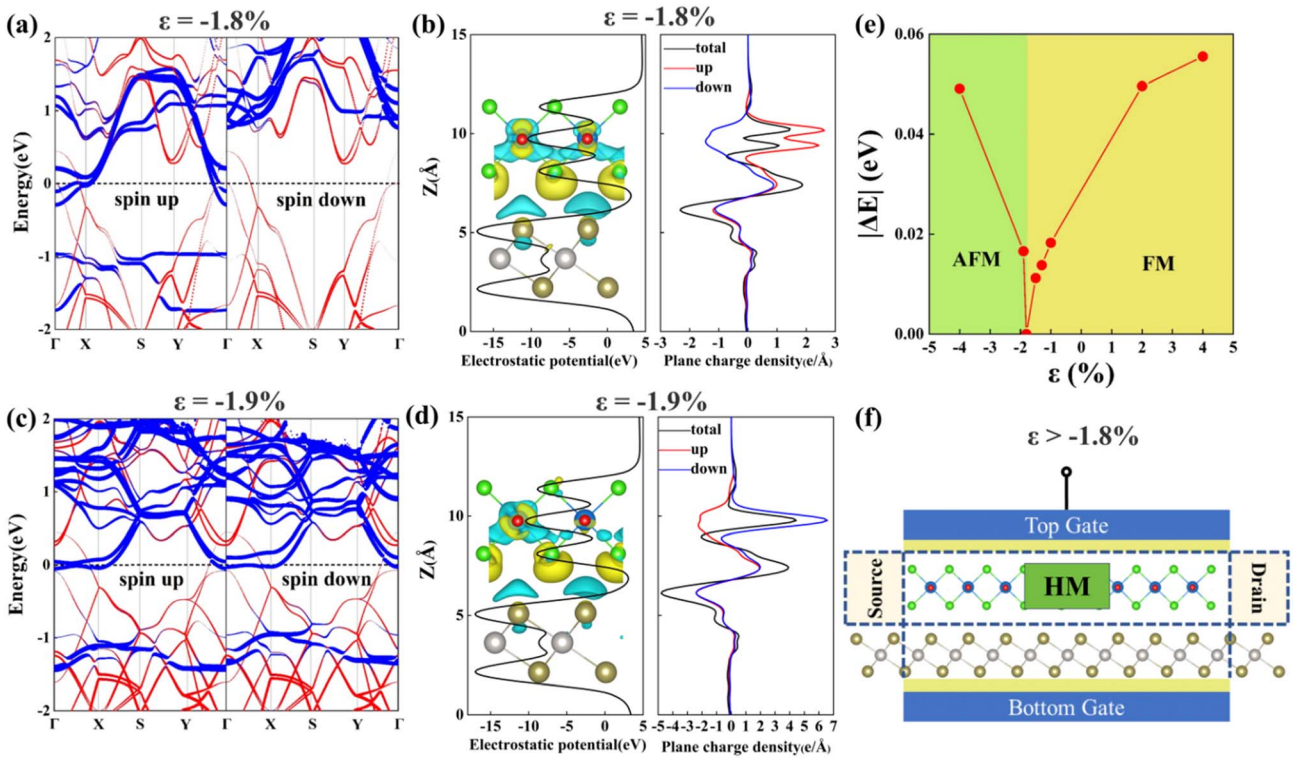

Fig. 6 Spin-resolved band structures, electrostatic potential, and charge density along *z* direction for $VOCl_2/PtTe_2$ heterostructure under (a and b) 1.8% and (c and d) 1.9% biaxial compressive strains, respectively. The contributions from $PtTe_2$ monolayer and $VOCl_2$ monolayer are represented by red and blue colours, respectively. (e) Magnetic ground states of the $VOCl_2/PtTe_2$ heterostructure under different biaxial strains, where $|\Delta E|$ denotes the absolute value of the energy difference between the FM state and the lowest energy AFM state. (f) The schematic plot of the field-effect spin filter of the $VOCl_2/PtTe_2$ heterostructure.

$$J_1 = -(E_{FM} - E_{AFM1} + E_{AFM2} - E_{AFM3})/4|S|^2 \quad (8)$$

$$J_2 = -(E_{FM} + E_{AFM1} - E_{AFM2} - E_{AFM3})/4|S|^2 \quad (9)$$

$$J_3 = -(E_{FM} - E_{AFM1} - E_{AFM2} + E_{AFM3})/8|S|^2 \quad (10)$$

Here, the values of J_1, J_2 and J_3 are calculated to be 0.037 eV, 0.001 eV and 0.003 eV, respectively. In Fig. 3(g), we further calculated the specific heat (C_V) as a function of the temperature from 0 K to 400 K. It is shown that the specific heat reaches a maximum at around 111 K and then decreases rapidly with the temperature further increases, indicating that the T_C of the heterostructure is about 111 K. It is known that $VOCl_2$ monolayer is AFM semiconductor with Néel temperature of 177 K based on Ising model,[59] which will overestimate the magnetic transition temperature. Therefore, it is believed that by forming $VOCl_2/PtTe_2$ heterostructure, an AFM-FM transition occurs and the magnetic transition temperature is almost unchanged.

To explore the electronic properties of the structure, spin-polarized band structures of $VOCl_2/PtTe_2$ heterostructure are plotted in Fig. 5(a) and (b), and the heterostructure is revealed to be FM metal with bands in both spin channels crossing Fermi level. Specially, $PtTe_2$ sublayer becomes to be nonmagnetic metal with the Fermi level down shifted, while $VOCl_2$ sublayer is turned to be FM half metal, which the electrons are conducting in the spin-up channel and insulating in the spin-down channel. The density of states (DOS) of $VOCl_2/PtTe_2$ heterostructure is shown Fig. 5(c), which suggests that the states near the Fermi level are mainly from $VOCl_2$ sublayer. Detailed orbital component analyses show that V-d_{xy} and d_{yz} orbitals contribute predominant. In addition, we calculate the band structures with different magnetization directions by including SOC effect, as shown in Fig. 5(d)–(f), which suggest that SOC effect has little effect on the electronic properties for $VOCl_2/PtTe_2$ heterostructure.

Finally, we discuss the effects of biaxial strains on the electronic and magnetic properties of $VOCl_2/PtTe_2$ heterostructure. We consider the strains from $\varepsilon = -4\%$ compressive strain to $\varepsilon = 4\%$ tensile strain, which is defined as $\varepsilon = (L - L_0)/L_0$, L and L_0 are the lattice constants in freestanding and strained states, respectively. Our results indicate that the heterostructure remains FM ground state under biaxial tensile strains ($\varepsilon > 0$), but undergoes FM state to AFM state transition when applying biaxial compressive strains ($\varepsilon < 0$) at around 1.81% (see Fig. 6(e)). The spin polarized band structures of the $VOCl_2/PtTe_2$ heterostructure under 1.8% and 1.9% biaxial compressive strains around the phase transition point are depicted in Fig. 6(a) and (c). Clearly, the system remains FM metallic property at smaller compressive strain ($\varepsilon > -1.81\%$), however, it changes to be AFM metal at higher strains ($\varepsilon < -1.81\%$). To be specific, the "$VOCl_2$" sublayer displays FM half metal property under smaller biaxial compressive strain ($\varepsilon > -1.81\%$), which is

transformed to be AFM metal under larger compressive strain ($\varepsilon < -1.81\%$). Such transition may arise from the structure distortion under strains, which further lead to the variation in exchange interactions in the heterostructure. Fig. 6(b) and (d) plot the electrostatic potential and plane charge density of the heterostructure at biaxial compressive strains of −1.8% and −1.9%, respectively. It is shown that a bit smaller charge transfer is found in the interlayer of $VOCl_2/PtTe_2$ under larger compressive strain. Therefore, the $VOCl_2/PtTe_2$ heterostructure can be used to design a field-effect spin filter as shown in Fig. 6(f), we can obtain a fully spin-polarized current by using "$VOCl_2$" sublayer when a non-spin-polarized current is input and the $VOCl_2/PtTe_2$ heterostructure is under tensile strain or compressive strains ($\varepsilon > -1.81\%$). Thus, the heterostructure can be a potential candidate for application in electrically controlled spintronics device.

Conclusions

In this work, we investigated the structure, magnetic, and electronic properties of two dimensional $VOCl_2/PtTe_2$ heterostructure by first-principles calculations. The results show that the $VOCl_2/PtTe_2$ heterostructure has FM ground state with the Curie temperature of about 111 K, higher than that of many 2D intrinsic FM materials. The band structure of the $VOCl_2/PtTe_2$ heterostructure is FM metal, in which the $VOCl_2$ "sublayer" shows to be FM half metal, and $PtTe_2$ "sublayer" shows to be nonmagnetic metal. Moreover, FM metal to AFM metal transition can be occurred by applying biaxial compressive strains larger than 1.81%. Our results provided an effective way on the property regulation of 2D electronic devices.

Author contributions

Conceptualization, Zhonghua Qian, Jie Ji and Licheng Wang; validation – Liyan Qian; formal analysis, Yuxuan Mao; data curation – Jie ji, Suchen Yao, and Jingyi Xu; writing – original draft preparation, Zhonghua Qian, Jie Ji; writing – original draft, supervision, Licheng Wang; review & editing, project administration, Xiuyun Zhang.

Conflicts of interest

There are no conflicts to declare.

Acknowledgements

This work is supported by the National Natural Science Foundation of China (41975062).

References

1 S. A. Wolf, D. D. Awschalom, R. A. Buhrman, J. M. Daughton, S. von Molnar, M. L. Roukes, A. Y. Chtchelkanova and D. M. Treger, *Science*, 2001, **294**, 1488–1495.
2 I. Zutic, J. Fabian and S. Das Sarma, *Rev. Mod. Phys.*, 2004, **76**, 323–410.
3 A. Fert, *Rev. Mod. Phys.*, 2008, **80**, 1517–1530.
4 S. D. Bader and S. S. P. Parkin, i, *Annu. Rev. Condens. Matter Phys.*, 2010, **1**, 71–88.
5 L. F. Wang, B. Wu, J. S. Chen, H. T. Liu, P. A. Hu and Y. Q. Liu, *Adv. Mater.*, 2014, **26**, 1559–1564.
6 Q. H. Wang, K. Kalantar-Zadeh, A. Kis, J. N. Coleman and M. S. Strano, *Nat. Nanotechnol.*, 2012, **7**, 699–712.
7 L. Li, F. Yang, G. J. Ye, Z. Zhang, Z. Zhu, W. Lou, X. Zhou, L. Li, K. Watanabe, T. Taniguchi, K. Chang, Y. Wang, X. H. Chen and Y. Zhang, *Nat. Nanotechnol.*, 2016, **11**, 593–597.
8 H. Wang, F. Fan, S. Zhu and H. Wu, *Europhys. Lett.*, 2016, **114**, 47001.
9 K. Zollner, M. Gmitra and J. Fabian, *New J. Phys.*, 2018, **20**, 073007.
10 Z. W. Zhang, J. Z. Shang, C. Y. Jiang, A. Rasmita, W. B. Gao and T. Yu, *Nano Lett.*, 2019, **19**, 3138–3142.
11 X. H. Cai, T. C. Song, N. P. Wilson, G. Clark, M. H. He, X. O. Zhang, T. Taniguchi, K. Watanabe, W. Yao, D. Xiao, M. A. McGuire, D. H. Cobden and X. D. Xu, *Nano Lett.*, 2019, **19**, 3993–3998.
12 E. Gerber, Y. Yao, T. A. Arias and E. A. Kim, *Phys. Rev. Lett.*, 2020, **124**, 106804.
13 W. O. Chen, Z. Y. Sun, Z. J. Wang, L. H. Gu, X. D. Xu, S. W. Wu and C. L. Gao, *Science*, 2019, **366**, 983–987.
14 Y. J. Zhang, X. H. Wu, B. B. Lyu, M. H. Wu, S. X. Zhao, J. Y. Chen, M. Y. Jia, C. S. Zhang, L. Wang, X. W. Wang, Y. Z. Chen, J. W. Mei, T. Taniguchi, K. Watanabe, H. G. Yan, Q. H. Liu, L. Huang, Y. Zhao and M. Y. Huang, *Nano Lett.*, 2020, **20**, 729–734.
15 M. Abramchuk, S. Jaszewski, K. R. Metz, G. B. Osterhoudt, Y. P. Wang, K. S. Burch and F. Tafti, *Adv. Mater.*, 2018, **30**, 1801325.
16 Y. J. Deng, Y. J. Yu, Y. C. Song, J. Z. Zhang, N. Z. Wang, Z. Y. Sun, Y. F. Yi, Y. Z. Wu, S. W. Wu, J. Y. Zhu, J. Wang, X. H. Chen and Y. B. Zhang, *Nature*, 2018, **563**, 94–99.
17 T. B. Prayitno and F. Ishii, *J. Phys. Soc. Jpn.*, 2019, **88**, 104705.
18 H. N. Liu, X. S. Wang, J. X. Wu, Y. S. Chen, J. Wan, R. Wen, J. B. Yang, Y. Liu, Z. G. Song and L. M. Xie, *ACS Nano*, 2020, **14**, 10544–10551.
19 H. C. Han, H. L. Zheng, Q. S. Wang and Y. Yan, *Phys. Chem. Chem. Phys.*, 2020, **22**, 26917–26922.
20 Y. Y. Zhu, H. L. Li, T. Chen, D. S. Liu and Q. H. Zhou, *Vaacuum*, 2020, **182**, 109694.
21 Z. P. Yan, N. N. Li, L. Y. Wang, Z. H. Yu, M. T. Li, J. B. Zhang, X. D. Li, K. Yang, G. Y. Gao and L. Wang, *J. Phys. Chem. C*, 2020, **124**, 23317–23323.
22 P. A. Joy and S. Vasudevan, *Phys. Rev. B: Condens. Matter Mater. Phys.*, 1992, **46**, 5425–5433.
23 A. R. Wildes, V. Simonet, E. Ressouche, R. Ballou and G. J. McIntyre, *J. Phys.: Condens.Matter*, 2017, **29**, 455801.
24 R. Gusmeao, Z. Sofer and M. Pumera, *Adv. Funct. Mater.*, 2019, **29**, 1805975.
25 D. Vaclavkova, A. Delhomme, C. Faugeras, M. Potemski, A. Bogucki, J. Suffczynski, P. Kossacki, A. R. Wildes, B. Gremaud and A. Saul, *2D Mater.*, 2020, **7**, 035030.

26 C. T. Kuo, M. Neumann, K. Balamurugan, H. J. Park, S. Kang, H. W. Shiu, J. H. Kang, B. H. Hong, M. Han, T. W. Noh and J. G. Park, *Sci. Rep.*, 2016, **6**, 20904.
27 K. Z. Du, X. Z. Wang, Y. Liu, P. Hu, M. I. B. Utama, C. K. Gan, Q. H. Xiong and C. Kloc, *ACS Nano*, 2016, **10**, 1738–1743.
28 T. L. Zhang, Y. M. Wang, H. X. Li, F. Zhong, J. Shi, M. H. Wu, Z. Y. Sun, W. F. Shen, B. Wei, W. D. Hu, X. F. Liu, L. Huang, C. G. Hu, Z. C. Wang, C. B. Jiang, S. X. Yang, Q. M. Zhang and Z. Qu, *ACS Nano*, 2019, **13**, 11353–11362.
29 N. H. Miao, B. Xu, L. G. Zhu, J. Zhou and Z. M. Sun, *J. Am. Chem. Soc.*, 2018, **140**, 2417–2420.
30 X. J. Yao and X. Y. Zhang, *J. Mater. Chem. C*, 2020, **8**, 14805–14811.
31 Y. Sun, Y. Y. Duan, X. Y. Li, X. K. Xu, X. J. Yao, S. Y. Liu, H. B. Yin, B. Wang, Y. J. Liu and X. Y. Zhang, *Int. J. Quantum Chem.*, 2023, **123**, e27117.
32 Y. X. Lin, L. Shi, Y. Chen, X. J. Yao, L. J. Meng, Y. Han, X. L. Zhao, M. S. He, Y. J. Liu and X. Y. Zhang, *Chem.–Eur. J.*, 2023, **29**, e202202925.
33 T. Jungwirth, X. Marti, P. Wadley and J. Wunderlich, *Nat. Nanotechnol.*, 2016, **11**, 231–241.
34 S. J. Gong, C. Gong, Y. Y. Sun, W. Y. Tong, C. G. Duan, J. H. Chu and X. Zhang, *Proc. Natl. Acad. Sci. U. S. A.*, 2018, **115**, 8511–8516.
35 W. Z. Wu, L. Wang, Y. L. Li, F. Zhang, L. Lin, S. M. Niu, D. Chenet, X. Zhang, Y. F. Hao, T. F. Heinz, J. Hone and Z. L. Wang, *Nature*, 2014, **514**, 470–474.
36 S. X. Yang, Y. J. Chen and C. B. Jiang, *Infomat.*, 2021, **3**, 397–420.
37 S. Bertolazzi, J. Brivio and A. Kis, *ACS Nano*, 2011, **5**, 9703–9709.
38 X. Tan, S. Wang, Q. X. Zhang, J. X. He, S. Y. Chen, Y. S. Qu, Z. Z. Liu, Y. Tang, X. T. Liu, C. Wang, Q. Wang and Q. Liu, *Nanoscale*, 2023, **15**, 9297.
39 Y. C. Cheng, Z. Y. Zhu, W. B. Mi, Z. B. Guo and U. Schwingenschlögl, *BPhys. Rev. B: Condens. Matter Mater. Phys.*, 2013, **87**, 100401(R).
40 B. Li, T. Xing, M. Zhong, L. Huang, N. Lei, J. Zhang, J. Li and Z. Wei, *Nat. Commun.*, 2017, **8**, 1958.
41 L. Yang, M. H. Wu and K. L. Yao, *Nanotechnology*, 2018, **29**, 215703.
42 B. J. Wang, Y. Y. Sun, J. Chen, W. W. Ju, Y. P. An and S. J. Gong, *J. Mater. Chem. C*, 2021, **9**, 3562–3568.
43 Y. Yamasaki, R. Moriya, M. Arai, S. Masubuchi, S. Pyon, T. Tamegai, K. Ueno and T. Machida, *2D Mater.*, 2017, **4**, 041007.
44 M. Gurram, S. Omar and B. J. van Wees, *Nat. Commun.*, 2017, **8**, 248.
45 J. B. S. Mendes, O. A. Santos, L. M. Meireles, R. G. Lacerda, L. H. Vilela-Leao, F. L. A. Machado, R. L. Rodriguez-Suarez, A. Azevedo and S. M. Rezende, *Phys. Rev. Lett.*, 2015, **115**, 226601.
46 Y. Guo, X. Yu, Y. H. Zhang, X. W. Zhang, S. J. Yuan, Y. F. Li, S. Y. A. Yang and J. L. Wang, *ACS Nano*, 2022, **16**, 11174–11181.
47 M. J. Yang, H. B. Shu, P. T. Tang, P. Liang, D. Cao and X. S. Chen, *ACS Appl. Mater. Interfaces*, 2021, **13**, 8764–8773.
48 T. Guo, Y. Liu, Y. Sun, S. Zhang, X. Xu, L. Wang, W. Zhou, Y. Liu, X. Yao and X. Zhang, *Appl. Phys. Lett.*, 2023, **122**, 192403.
49 G. Kresse and J. Furthmüller, *Comput. Mater. Sci.*, 1996, **6**, 15–50.
50 W. Kohn and L. J. Sham, *Phys. Rev.*, 1965, **140**, A1133–A1138.
51 P. Honhenberg and W. Kohn, *Phys. Rev.*, 1964, **136**, B864–B871.
52 J. P. Perdew, K. Burke and M. Ernzerhof, *Phys. Rev. Lett.*, 1996, **77**, 3865.
53 P. E. Blochl, *Phys. Rev. B: Condens. Matter Mater. Phys.*, 1994, **50**, 17953.
54 S. Grimme, *J. Comput. Chem.*, 2004, **25**, 1463–1473.
55 S. L. Dudarev, G. A. Botton, S. Y. Savrasov, C. J. Humphreys and A. P. Sutton, *Phys. Rev. B: Condens. Matter Mater. Phys.*, 1998, **57**, 1505.
56 X. Liu, A. P. Pyatakov and W. Ren, *Phys. Rev. Lett.*, 2020, **125**, 247601.
57 X. Yao, L. Wang, Y. Sun, X. Li, J. Sun, B. Wang, M. He and X. Zhang, *Phys. Rev. B*, 2022, **105**, 214421.
58 F. Wu, X. Yao, Y. Liu, X. Zhu, J. Lu, W. Zhou and X. Zhang, *Nanoscale*, 2023, **15**, 2079–2086.
59 H. Ai, X. Song, S. Qi, W. Li and M. Zhao, *Nanoscale*, 2019, **11**, 1103–1110.
60 L. H. Han, Y. Y. Zou, Q. M. Zeng, X. N. Guan, B. N. Jia, Y. P. Gao, G. Liu and L. Y. Wu, *J. Solid State Chem.*, 2022, **305**, 122657.
61 J. B. Goodenough, *Phys. Rev.*, 1955, **100**, 564.
62 J. Kanamori, *J. Appl. Phys.*, 1960, **31**, S14.
63 P. W. Anderson, *Phys. Rev.*, 1959, **115**, 2.
64 T. Burkert, L. Nordstrom, O. Eriksson and O. Heinonen, *Phys. Rev. Lett.*, 2004, **93**, 027203.